Guided optical modes in randomly textured ZnO thin films imaged by near-field scanning optical microscopy

K. Bittkau* and R. Carius
Institut für Photovoltaik, Forschungszentrum Jülich GmbH, 52425 Jülich, Germany

C. Lienau
Max-Born-Institut für Nichtlineare Optik und Kurzzeitspektroskopie, Max-Born-Strasse 2A, 12489 Berlin, Germany
and Institut für Physik, Carl von Ossietzky Universität Oldenburg, 26111 Oldenburg, Germany
(Received 30 June 2006; revised manuscript received 13 February 2007; published 24 July 2007)

We report on near-field optical imaging of light transmission through textured zinc oxide (ZnO) thin films grown on glass substrates. Such ZnO layers are commonly used as a transparent conducting oxide for the front contacts in thin-film solar cells. To increase the quantum efficiency of such solar cells, the ZnO surface is randomly textured, resulting in a higher light scattering and promoting light trapping. Here, we study these phenomena microscopically by imaging the local optical mode profiles in such thin films. Our results give clear evidence for the interconversion of propagating and guided evanescent modes. Such information, which cannot be extracted from more conventional far-field optical studies, may prove helpful in further optimizing the efficiencies of thin-film optoelectronic devices.

DOI: 10.1103/PhysRevB.76.035330 PACS number(s): 78.66.Li, 78.68.+m, 42.25.Fx, 73.50.Pz

I. INTRODUCTION

The localization of light in strongly scattering, random dielectric media is one of the most intriguing phenomena in optics, attracting the interest of experimental and theoretical physicists alike.[1–3] It is not only a fascinating and controversially discussed fundamental physical effect but also of immediate practical relevance. In particular, when designing thin-film solar cells and light emitting diodes (LEDs), randomly textured dielectric surfaces are often used to enhance the external quantum efficiencies of these devices.

Specifically, in GaAs-based thin-film LEDs, scattering at textured surfaces enhances the outcoupling of light which is otherwise totally internally reflected within the high refractive index semiconductor and thus increases the efficiency compared to devices with flat surfaces.[4,5] In thin-film photovoltaics, external quantum efficiencies strongly depend on the trapping of light resulting from multiple reflections, and hence textured surfaces are well known to enhance solar cell efficiencies.[6–8]

Consequently, the optimization of surface structure is one of the most important challenges in thin-film photovoltaic research. Mostly, far-field optical techniques are used to characterize scattering efficiencies.[9–11] With these techniques, correlations between roughness parameters and scattering properties, e.g., the haze and angular distribution function, and also correlations between scattering properties and solar cell efficiencies can be studied. Some principle trends can be found, but it is well known that these statistical parameters cannot describe the enhancement of external quantum efficiency in full detail. The reason is that such experiments, however, are not directly sensitive to diffraction processes on a subwavelength scale and the resulting generation of evanescent waves and, therefore, can provide only limited insight. Near-field based techniques, however, are particularly sensitive to such scattering phenomena and allow—in favorable cases—for a direct imaging of the local optical density of states,[12–14] similar to imaging of the local electronic density of states in scanning tunneling microscopy.[15–17] Thus, it can be expected that near-field spectroscopic studies can provide new insight into the optical properties of textured thin films[18] relevant for the optimization of solar cell efficiencies. So far, near-field investigations of ZnO structures have been reported for lasing nanowires[19,20] and isolated ZnO nanorod single-quantum-well structures.[21] It is the aim of this paper to present near-field studies of ZnO layers relevant for solar cell applications and, in particular, to explore what new information can be gained from such studies.

In this paper, near-field optical studies of light transmission through randomly textured ZnO thin-film solar-cell materials are reported. Numerical calculations of the electric field intensity by using a rigorous solution of Maxwell's equations are performed to describe the experimental near-field intensity. Our results give evidence for the conversion of propagating far-field light into evanescent modes guided within subwavelength sized topographical structures at the surface of the thin film. In the optical near field, side maxima of the guided optical modes are found in a subwavelength vicinity of the main maximum. For larger distances, in the optical far-field regime, the optical mode profile is converted into a specklelike transmission image which indicates that randomly scattering processes are indeed important for the optical properties of these films.

II. EXPERIMENT

The textured ZnO thin films are prepared by sputtering ZnO layers with a thickness of 1 μm on a glass substrate. The samples are then etched in a diluted HCl solution to create a random rough surface with a rms roughness of about 150 nm, resulting in a total surface corrugation of about 1 μm. Such films are commonly used as transparent conducting oxide for the front contacts in thin-film solar cells

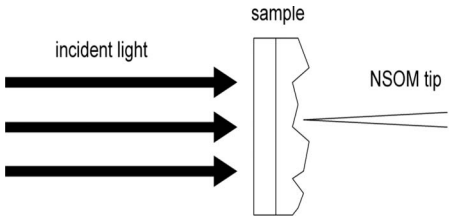

FIG. 1. Schematic view of the collection-mode geometry of NSOM. The incident laser beam illuminates the sample from the substrate side. The transmitted intensity is collected with the fiber tip.

and are, therefore, the first medium of the multilayer structures in solar cells. The optical properties of those ZnO films are important for light coupling into the solar cell.

Here, light transmission through such textured films is microscopically studied by means of near-field scanning optical spectroscopy. The experiments are performed in a homebuilt variable temperature near-field scanning optical microscope (NSOM) operated in a transmission geometry at room temperature (Fig. 1). The experimental setup is described in detail in Ref. 22. Different monochromatic, continuous-wave laser sources at wavelengths λ of 488, 658, and 780 nm are used to illuminate the sample at normal incidence. The laser beams are weakly focused to a spot size of about 150 μm onto the substrate side of the sample, which is held fixed in space. The transmitted light is then collected on the thin-film side using a commercial aluminum-coated near-field fiber probe (Veeco) with an aperture diameter of less than 80 nm. We have independently verified that these tips indeed give sub-100-nm optical resolution by imaging transmission near field through a Fischer test pattern (Kennex) in the same collection geometry.[23] The light collected with the single-mode fiber probe is imaged onto a cooled photomultiplier tube. Lock-in detection at a modulation frequency of 3.1 kHz is used for noise rejection.

The near-field fiber probe is mounted on a quartz tuning fork, oscillating at 32 kHz connected to two small, high resonance frequency multilayer piezoactuators (Physik Instrumente, PICMA) with a scan range of 4 μm and a hardware linearized three axis scanner with a scan range of $100 \times 100 \times 100$ μm^3 (Physik Instrumente, NanoCube). The high resonance frequency z piezo is used together with a conventional shear-force feedback setup[24] for keeping the tip-to-sample distance constant at about 20 nm. The NanoCube is used for two-dimensional lateral, i.e., x-y, scanning of the tip relative to the sample. In addition to such constant-distance scans, constant-height scans are also performed, disengaging the distance control and keeping the z position of the tip constant. Care is taken to keep the tilt of the selected sample area as small as possible. Due to the fairly pronounced surface roughness of the textured films (on the order of 150 nm rms), the tip-to-sample distance varies in these constant-height scans by about 1 μm from minimum to maximum. Therefore, the tip-to-sample distance in the constant-height scans varies according to the topographic structure. To avoid tip-sample contact in short-distance constant-height scans, i.e., for scanning heights smaller than the sample corrugation, the shear-force feedback is engaged when the tip-to-sample distance becomes smaller then 20 nm. Here, the distance-control loop becomes effective and retracts the tip whenever necessary.

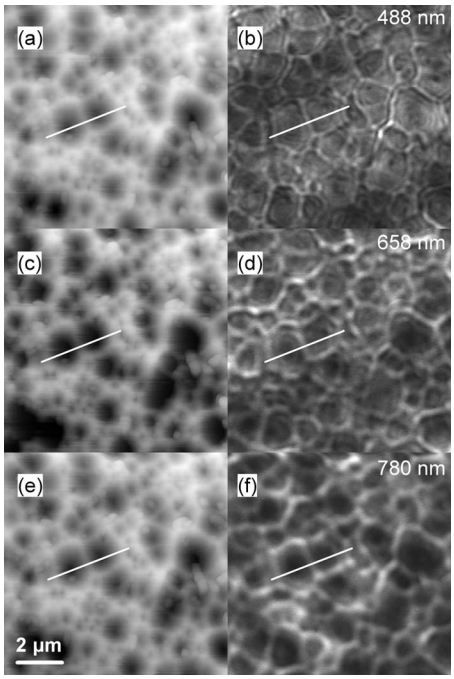

FIG. 2. [(a), (c), and (e)] Topography and [(b), (d), and (f)] NSOM transmission images at laser wavelengths of 488, 658, and 780 nm, respectively, in constant-distance mode. The white lines in the topographic images represent the positions for the cross sections in Fig. 3.

It is important that the mechanical stability of our NSOM system is sufficiently high to repeat experiments at different wavelengths and/or tip-to-sample distances with only minor tip-to-sample drifts, even over a time scale of several days. This is, of course, particularly important for ensuring comparability of different constant-height scans which do not provide independent topography information.

III. RESULTS AND DISCUSSION

Figure 2 shows topographic images [(a), (c), and (e)] and the corresponding NSOM transmission images [(b), (d), and (f)] recorded in constant-distance mode at laser wavelengths of $\lambda = 488$, 658, and 780 nm, respectively. In all three cases, the topography and the corresponding NSOM images are measured simultaneously. The total corrugation seen in the topographic images is about 1 μm. In these images, the sample tilt is not corrected. The signal modulation of the near-field transmission images is close to 100%. The measurements for different wavelengths have been performed at different days.

The topographic experiments reveal a craterlike surface with evenly distributed craters of different heights—ranging approximately between 50 and 800 nm—and different widths—ranging from a few tens of nanometers up to slightly more than 1 μm. The most pronounced feature of the corresponding NSOM transmission images is a clear

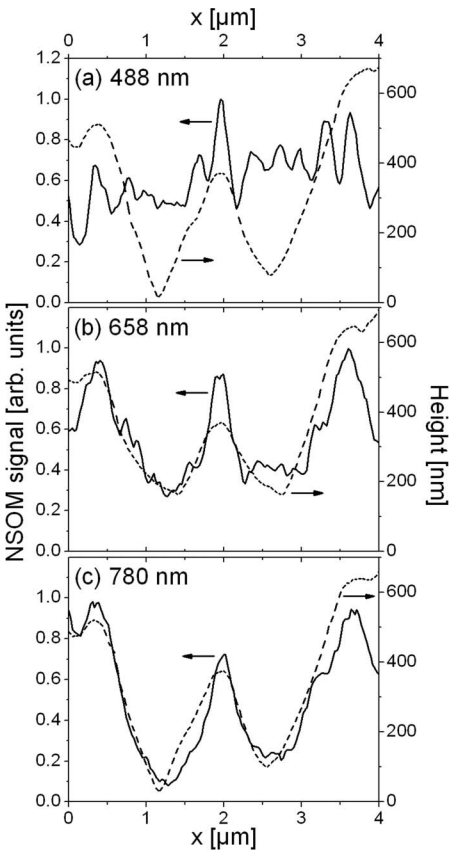

FIG. 3. Cross sections of the topography and the NSOM transmission at laser wavelength of (a) 488 nm, (b) 658 nm, and (c) 780 nm in constant-distance mode. The positions for the cross sections are depicted in Fig. 2 by the white lines.

ringlike structure of the transmission maxima, spatially correlated to the topographic structure of the sample. The highest transmission intensities are found at the vertices and rims of the surface topography (see the topography cross sections shown in Fig. 3 along the white lines indicated in Fig. 2). At all wavelengths, the optical transmission peaks are surprisingly strongly localized on a subwavelength scale. Cross sections through the NSOM images along the same line as in Fig. 2 are shown in Fig. 3 for the three different wavelengths. With increasing wavelength, the full width at half maximum of the transmission maxima increases from ~200 nm at $\lambda = 488$ nm [Fig. 3(a)] to ~320 nm at $\lambda = 780$ nm [Fig. 3(c)].

The ratio I_m/I_{av} between the maximum local intensity $I_m = \max(I(x,y))$ and the average intensity $I_{\mathrm{av}} = \langle I(x,y)\rangle$, where $\langle\ \rangle$ denotes the spatial average, is taken as a measure of the local field enhancement in these images, assuming that I_{av} equals the total far-field transmittance of the sample. By analyzing several images for each wavelength, enhancements of about ~9 at $\lambda = 488$ nm, ~7 at $\lambda = 658$ nm, and ~5 at $\lambda = 780$ nm are found. These values reflect the most pronounced increase of the local transmittance near the rims. On average, the rims show an enhancement of about 3–4, independent of the excitation wavelength.

In addition to the coarse ringlike structure at the topographic vertices, the NSOM images reveal a fine structure, which looks like rings that lie inside the coarse structure. The

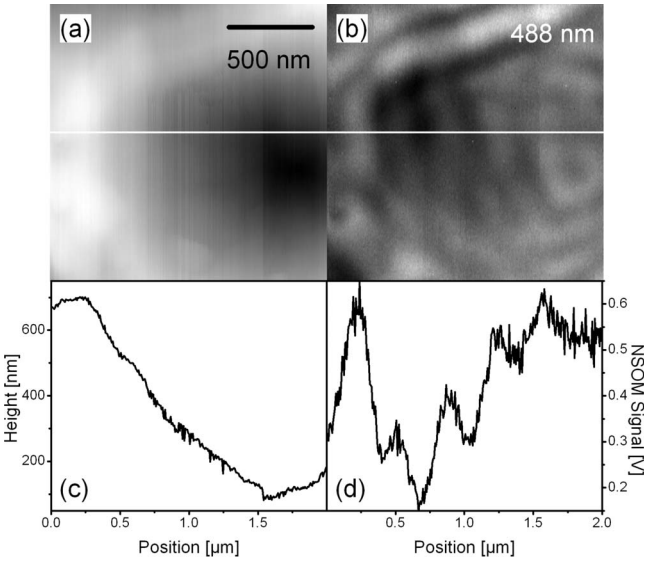

FIG. 4. (a) Topography and (b) NSOM transmission image at 488 nm in constant-distance mode. (c) and (d) represent cross sections from (a) and (b), respectively.

contrast of these ringlike features is most pronounced at shorter wavelength [$\lambda = 488$ nm, Fig. 3(a)] and seems to disappear at longer wavelengths [$\lambda = 780$ nm, Fig. 3(c)].

To provide a better insight into this fine structure, a detailed, highly spatially resolved scan taken at a wavelength of 488 nm is shown in Fig. 4. The topography in (a) shows a single crater-shaped pit with a height difference between rim and center of about 750 nm. The optical signal (b) shows the transmission enhancement at the rim of the crater and the ringlike structure inside the crater. For a better comparison, cross sections from (a) and (b) are depicted in (c) and (d), respectively. At first sight, the fine structure seems to be a periodic recurrence of the strong response at the rim. By comparing different craters, the recurrence period is found to depend mainly on the slope of the surface profile.

It is proposed that the fine structure yields from laterally guided optical modes within the rims of the craters in the ZnO layer. These modes are excited by scattering of the incident light at the subwavelength topographic features and induce an evanescent electric field in air. Evanescent fields are characterized by an in-plane component of the wave vector $k_{\parallel}$, which is larger than the absolute value $k = 2\pi/\lambda$. This leads to an imaginary out-of-plane component $k_z = (k^2 - k_{\parallel}^2)^{1/2}$. For in-plane components $k_{\parallel}$ smaller than the absolute value k, the mode can couple to propagating modes in air. Therefore, only modes which are evanescent in air are guided in the ZnO layer. These modes decrease exponentially in air with increasing distance to the surface and can, therefore, only be measured in the near field of the structure and vanish at distances on the order of half the wavelength. In thin-film solar cells, guidance of light is a great challenge to increase the absorbance and therefore the energy conversion efficiency.

To support this interpretation, the evolution of the electric field intensity of the thin-film optical modes with increasing distance from the sample surface is studied by taking near-

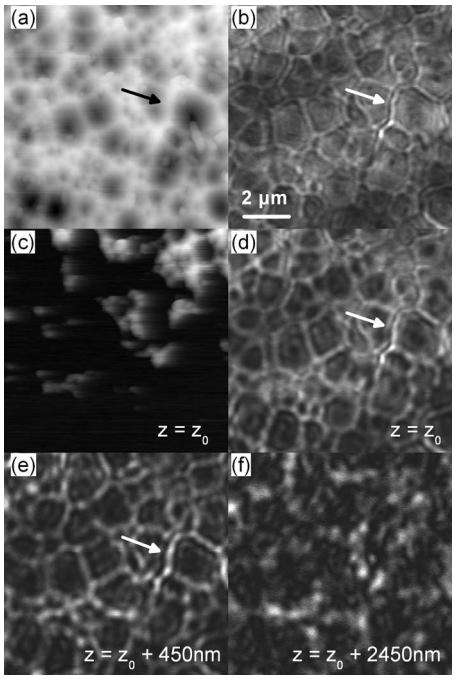

FIG. 5. (a) Topography and (b) NSOM transmission images at 488 nm in constant-distance mode. (c) shows the topographic information for the mixed scanning mode at the base height z_0. The corresponding NSOM image is shown in (d). (e) and (f) represent the NSOM images in constant-height mode for the heights z_0 +450 nm and z_0+2450 nm, respectively. The arrows mark a special structure described in text.

field transmission measurements at different distances between the near-field fiber probe and sample surface. The results for a laser wavelength of 488 nm are shown in Fig. 5. Figures 5(a) and 5(b) represent, respectively, the topography and the NSOM image in constant-distance mode. The images are identical to those in Figs. 2(a) and 2(b). The total sample tilt for this scan area is found to be 250 nm, corresponding to a tilt angle of 1°. Figure 5(c) shows the topographic image taken in the mixed scanning mode. Here, the tip-to-sample distance is less than the total sample corrugation. Therefore, the tip height is kept constant when the tip-to-sample distance is larger than the shear-force feedback range of about 20 nm [black regions in Fig. 5(c)], whereas the feedback is engaged when the tip-to-sample distance becomes less than about 20 nm. At these positions, the image reflects the sample topography as in (a) with a reduced effective corrugation of 370 nm. The primary height in this mode is defined to be z_0 [approximately 150 nm larger than the average topography height in (a)]. Images at larger distances of z_0 +450 nm and z_0+2450 nm are taken in constant-height mode. The corresponding NSOM transmission images for the heights z_0, z_0+450 nm, and z_0+2450 nm are shown in Figs. 5(d)–5(f), respectively.

The distance dependent NSOM images essentially confirm the predicted scenario. The coarse structures in these images, i.e., the transmission peaks near the vertices of the surface topography, are spatially broadened with increasing distance from the surface. This broadening essentially reflects the loss in spatial resolution due to the finite distance

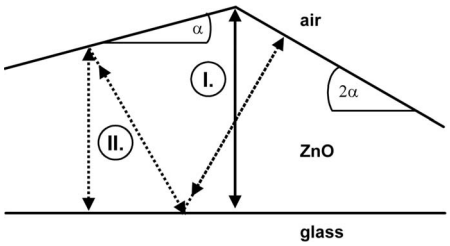

FIG. 6. Light rays in a textured thin film to illustrate two different interference effects marked as situations I. and II. described in text.

between near-field probe and sample. Three different distance regions are found in the experiment: (I) the near-field region, where both the coarse and the fine structure can be imaged, for tip-to-sample distances smaller than half the wavelength [Fig. 5(b) and parts of (d)]; (II) the intermediate region for distances up to a few times the wavelength [Fig. 5(e) and parts of (d)], where only the coarse structure can be observed; and (III) the far-field region, where the correlation between optical image and sample topography is greatly reduced [Fig. 5(f)] and, instead, a specklelike transmission image is found, as expected for such a randomly textured film.

For a better visualization of the distance dependence, arrows are added in Fig. 5 to mark a special position where the same coarse structure can be seen for the different tip-to-sample distances. On both sides of the coarse structure, a fine intensity modulation can be seen in the near field [Fig. 5(b)], which is significantly reduced in contrast at the beginning of the intermediate region [Fig. 5(d)] and vanishing in the middle of the intermediate region [Fig. 5(e)]. The suppression of this modulation for distances shorter than the wavelength of the incident light is a strong evidence for the evanescent nature of the corresponding optical modes and confirms their assignment to guided modes within the textured thin film.

Alternative interpretations of the experimentally observed data could be based on Fabry-Pérot effects. Let us first consider the coarse structure at the highest positions in topography. Here, the incident light from the substrate side is partially back reflected without any tilt angle and will be reflected again at the ZnO/glass interface (see situation I. in Fig. 6). This multiple reflection at the interfaces yields either constructive or destructive interference depending on the local layer thickness. One expect that, along the rim of a crater, the Fabry-Pérot effect pronounces an interference pattern, switching between darker and brighter regions in the optical transmission. Instead, a clear and bright transmission enhancement along the rims is always found in the experiment with only slight spatial modulations (Fig. 2). Therefore, it is improbable that the coarse structure at the rims results from multiple reflections at the interfaces.

Let us now consider the fine structure inside the craters. Here, the situation becomes more complicated due to the finite steepness of the textured surface. The incident light is back reflected at the surface with a significant tilt angle. Here, two different mechanisms are possible: first, a Fabry-Pérot-like effect from a multiple reflected light path inside the ZnO, layer which leads back to the original position at

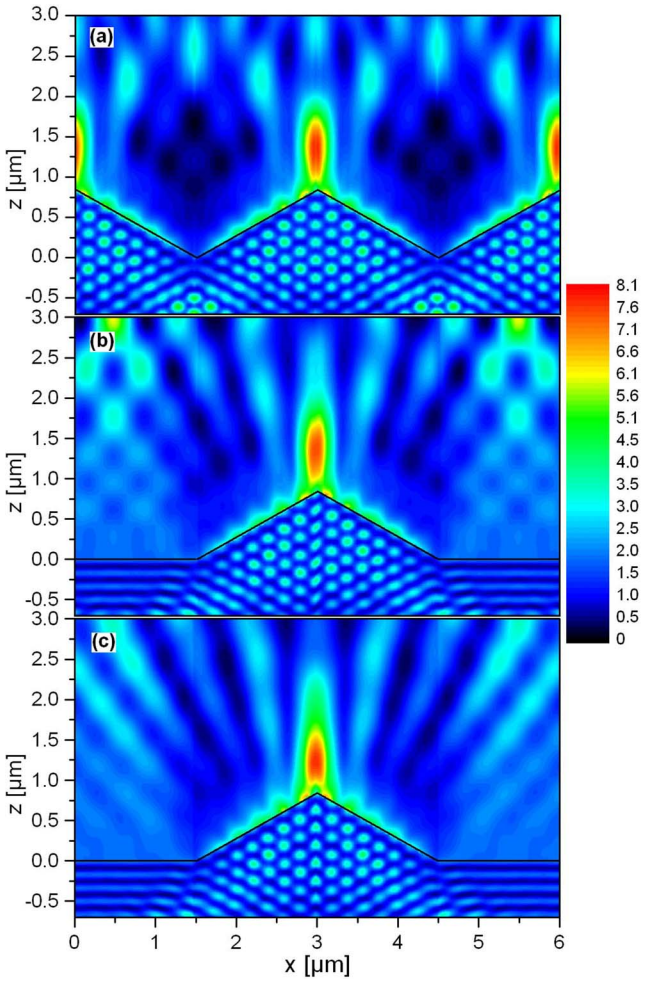

FIG. 7. (Color online) Calculated intensity of the electric field ($|E|^2$) for a periodic structure of triangular ridges with three different distances between the ridges. In (a), (b), and (c), the peak-to-peak distance is chosen to be 3, 5, and 18 μm, respectively. The intensity scale is normalized to the incident wave.

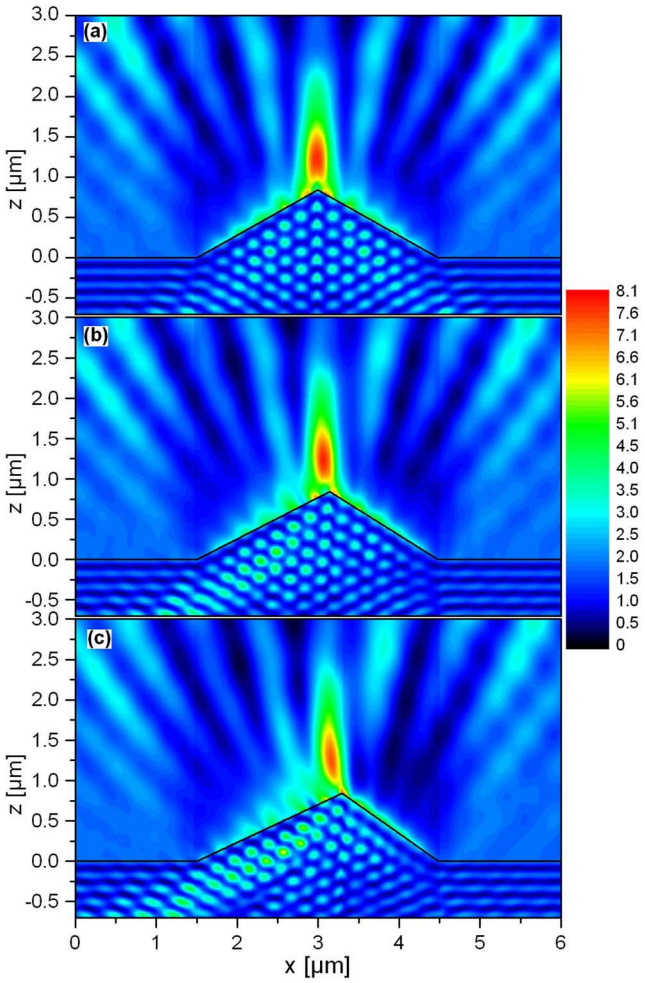

FIG. 8. (Color online) Calculated intensity of the electric field ($|E|^2$) for a periodic structure of triangular ridges with a distance of 18 μm between the ridges for three asymmetries. In (a), the field distribution for symmetric ridges is shown. In (b) and (c), the profiles of the ridges are chosen to be asymmetric with the strongest asymmetry in (c). The intensity scale is normalized to the incident wave.

the sample surface to achieve an interference (see situation II. in Fig. 6), and, second, an interference resulting from phase-coherent illumination of different positions of the sample. The superposition of all those rays may lead to an interference pattern correlated to the fine structure in the experiment.

The Fabry-Pérot-like effect can be ruled out to be the origin of the fine structure. To ensure a significant intensity modulation at one side of a rim with a steepness angle α, the other side of the rim must have a steepness angle of 2α for an incidence normal to the textured surface (see Fig. 6). Only in this case the light can back reflected to the origin position, but in the experiment, the fine structure is observed in many more cases.

The interference resulting from phase-coherent illumination of different positions of the sample can be eliminated experimentally by illuminating the sample with the near-field aperture of the fiber tip and detecting the light intensity transmitted in the far field. Then, only one illuminating ray exists and only Fabry-Pérot-like effects and internal optical modes affect the experimental results. In this illumination mode configuration, very similar images are measured with the strongest intensity at the highest topographic positions and a fine structure inside the craters.

In contrast, internal optical modes can be excited in both configurations, illumination and collection modes. To get a better insight of the mode profile inside the ZnO, electrodynamic calculations are performed by solving Maxwell's equations rigorously.[25,26] In our calculations, a periodic structure is chosen with triangular ridges along the y axis. The ridges have a total width of 3 μm and a total height of 850 nm. The ridges are described by a medium with a refraction index of $n=2$ on top of a half space with the same refraction index. Therefore, in these calculation, multiple reflections from the interfaces of the substrate are not taken into account. For all calculations, an incident plane wave is assumed with a wavelength of 658 nm, which illuminates the structure from the ZnO half space at normal incidence.

In Fig. 7, the calculated intensity of the electric field ($|E|^2$) for the simplified structure is shown for three different dis-

tances between the ridges. The calculated intensity patterns are in good agreement with the experiment. The strongest intensity is found at the highest point of the ridge and forms a laterally restricted jet. The fine structure in the near field is also found in the calculations. The electric field distribution depict a two-dimensional periodic pattern inside the ZnO ridge. To study the physical origin of the intensity profile in air and inside the ZnO, the structural parameters are varied. In Fig. 7, different distances between the peaks of the ridges are assumed. In (a), (b), and (c), the peak-to-peak distance, identical to the periodicity, is chosen to be 3, 5, and 18 μm, respectively.

With this variation, one can study the problem of whether interference effects of neighboring ridges are responsible for the observed intensity profile. Considering the ridges as microscopical light sources dominated by scattering processes, the distance between two ridges should strongly influence the intensity modulation. From Fig. 7, it is found that the distance between the ridges influences the far-field behavior strongly. However, the near-field behavior with the jet over the highest point and the modulated intensity directly over the surface are only influenced very weakly by the distance of the ridges.

The intensity profiles for different shapes of the ridges are calculated and shown in Fig. 8 for a periodicity of 18 μm. In (a), the field distribution for symmetric ridges is shown. In (b) and (c), the profile of the ridges are chosen to be asymmetric with the strongest asymmetry in (c). The asymmetry strongly influences the intensity profile in the near field. With increasing distortion, the near-field fine structure on the right-hand side of the ridge becomes weaker while the opposite intensity modulation becomes stronger. A strong correlation between the intensity pattern inside the ZnO ridge and the modulation of the near field in air is found especially for the strongest distortion of the structure [Fig. 8(c)], which leads to the conclusion that internal optical modes are responsible for the fine structure in the NSOM transmission data.

The calculations result in weakly bound optical states in the x-z plane with an independent and therefore free propagating component in the y direction. In the real three-dimensional textured sample, wave vectors in all directions are transferred. Therefore, laterally guided optical modes are generated along the ZnO rims.

IV. CONCLUSION

Transmission measurements on randomly textured ZnO layers are presented with very high spatial resolution using NSOM. The optical intensity is found to be strongly confined on a subwavelength scale. The highest intensities are always observed at the vertices and rims in the topography with five to nine times enhanced transmittance. The optical modes at the ZnO surface exhibit an evanescent part which decreases rapidly with tip-to-sample distance. The evanescent fields are correlated to a lateral fine structure in the NSOM images and represent the intensity profile of laterally guided optical modes close to the surface. This interpretation is assisted by numerical simulations. Fabry-Pérot-like effects and interferences resulting from phase-coherent illumination of different positions of the sample are ruled out to be the origin of this fine structure.

These laterally guided optical modes are strongly correlated with scattering processes. Due to the localization at sharp topographic structures, variation of the surface profile should have an influence on the guided modes and, therefore, on the light coupling and trapping in solar cells. Furthermore, future concepts may incorporate near-field enhancement effects which require a detailed knowledge about the field distribution. The experimentally found increase of transmittance shows significant variation between typical rims and the best rims. Thus, near-field studies give important insight into light propagation in textured ZnO and provide hints to improve light trapping for optimization of solar cell efficiency.

ACKNOWLEDGMENTS

We would like to thank S. Gewinner, R. Pomränke, and S. Schelm from the Max-Born-Institut for the development of the NSOM setup and the excellent instruction units use. Further, we would like to thank J. Hüpkes for providing the samples for this study.

*k.bittkau@fz-juelich.de

[1] *Photonic Crystals and Light Localization in the 21st Century*, edited by C. M. Soukoulis, NATO Science Series C Vol. 563 (Kluwer, Dordrecht, 2000).

[2] See, e.g., M. Gurioli, F. Bogani, L. Cavigli, H. Gibbs, G. Khitrova, and D. S. Wiersma, Phys. Rev. Lett. **94**, 183901 (2005), and references therein.

[3] D. S. Wiersma, P. Bartolini, A. Lagendijk, and R. Righini, Nature (London) **390**, 671 (1997).

[4] I. Schnitzer, E. Yablonovitch, C. Caneau, T. J. Gmitter, and A. Scherer, Appl. Phys. Lett. **63**, 2174 (1993).

[5] R. Windisch, B. Dutta, M. Kuijk, A. Knobloch, S. Meinlschmidt, S. Schoberth, P. Kiesel, G. Borghs, G. H. Döhler, and P. Heremans, IEEE Trans. Electron Devices **ED-47**, 1492 (2000).

[6] E. Yablonovitch and G. D. Cody, IEEE Trans. Electron Devices **ED-29**, 300 (1982).

[7] E. Yablonovitch, J. Opt. Soc. Am. **72**, 899 (1982).

[8] O. Kluth, B. Rech, L. Houben, S. Wieder, G. Schöpe, C. Beneking, H. Wagner, A. Löffl, and H. W. Schock, Thin Solid Films **351**, 247 (1999).

[9] A. Banerjee and S. Guha, J. Appl. Phys. **69**, 1030 (1991).

[10] P. Campbell, J. Opt. Soc. Am. B **10**, 2410 (1993).

[11] J. Krč, M. Zeman, O. Kluth, F. Smole, and M. Topič, Thin Solid Films **426**, 296 (2003).

[12] C. Chicanne, T. David, R. Quidant, J. C. Weeber, Y. Lacroute, E. Bourillot, A. Dereux, G. Colas des Francs, and C. Girard, Phys.

Rev. Lett. **88**, 097402 (2002).
[13] S. Grésillon, L. Aigouy, A. C. Boccara, J. C. Rivoal, X. Quelin, C. Desmarest, P. Gadenne, V. A. Shubin, A. K. Sarychev, and V. M. Shalaev, Phys. Rev. Lett. **82**, 4520 (1999).
[14] C. Ropers, D. J. Park, G. Stibenz, G. Steinmeyer, J. Kim, D. S. Kim, and C. Lienau, Phys. Rev. Lett. **94**, 113901 (2005).
[15] M. F. Crommie, C. P. Lutz, and D. M. Eigler, Science **262**, 218 (1993).
[16] M. F. Crommie, C. P. Lutz, and D. M. Eigler, Nature (London) **363**, 524 (1993).
[17] E. J. Heller, M. F. Crommie, C. P. Lutz, and D. M. Eigler, Nature (London) **369**, 464 (1994).
[18] V. Emiliani, F. Intonti, M. Cazayous, D. S. Wiersma, M. Colocci, F. Aliev, and A. Lagendijk, Phys. Rev. Lett. **90**, 250801 (2003).
[19] J. C. Johnson, H. Yan, R. D. Schaller, P. B. Petersen, P. Yang, and R. J. Saykally, Nano Lett. **2**, 279 (2002).
[20] P. Yang, H. Yan, S. Mao, R. Russo, J. Johnson, R. Saykally, N. Morris, J. Pham, R. He, and H.-J. Choi, Adv. Funct. Mater. **12**, 323 (2002).
[21] T. Yatsui, M. Ohtsu, J. Yoo, S. J. An, and G.-C. Yi, Appl. Phys. Lett. **87**, 33101 (2005).
[22] G. Behme, A. Richter, M. Süptitz, and Ch. Lienau, Rev. Sci. Instrum. **68**, 3458 (1997).
[23] Some of these test images are shown on www.mbi-berlin. de/de/research/projects/3-02/highlights/lt-snom/lt-snom-over.html, together with a more detailed explanation of the experimental setup.
[24] K. Karrai and R. D. Grober, Appl. Phys. Lett. **66**, 1842 (1995).
[25] J. Chandezon, D. Maystre, and G. Raoult, J. Opt. **11**, 235 (1980).
[26] J. Chandezon, M. T. Dupuis, G. Cornet, and D. Maystre, J. Opt. Soc. Am. **72**, 839 (1982).